Chemical Science

ROYAL SOCIETY OF CHEMISTRY

EDGE ARTICLE

View Article Online
View Journal | View Issue

Check for updates

Cite this: *Chem. Sci.*, 2025, **16**, 18869

All publication charges for this article have been paid for by the Royal Society of Chemistry

Received 1st July 2025
Accepted 5th September 2025

DOI: 10.1039/d5sc04862a

rsc.li/chemical-science

Simulations reveal a balance between protein–protein and protein–lipid interactions during condensation on membrane surfaces

Ketsia Zinga,[a] Yohan Lee,[a] Shireen Pathak,[a] Nishi Patel,[a]
Jeanne Stachowiak *[ab] and Pengyu Ren *[a]

Liquid–liquid phase separation of protein condensates occurs frequently on biological membranes, where it is involved in diverse physiological processes from cell–cell recognition to endocytosis. Several recent studies have suggested that binding to lipids promotes phase separation of proteins. However, relatively little is known about the underlying molecular mechanisms. Here we use coarse-grained molecular dynamics simulations, grounded by data from experiments, to investigate the condensation of intrinsically disordered proteins on membrane surfaces. Attaching polyampholytic intrinsically disordered proteins to membranes composed of lipids with neutral head groups resulted in spontaneous protein condensation and coarsening on membrane surfaces, in agreement with experimentally-derived phase diagrams. Introducing lipids with negatively charged head groups strengthened association of proteins with membranes. However, as the concentration of charged lipids increased, protein–lipid interactions began to compete with protein–protein interactions, driving protein condensates to disperse, as confirmed by experiments. Contrary to previous understanding, this work suggests that negatively charged membranes, which are found throughout the cell, can regulate protein condensation both positively and negatively, depending on the balance between protein–protein and protein–lipid interactions.

Introduction

Liquid–liquid phase separation (LLPS) of proteins is a phenomenon in which proteins spontaneously separate from a homogenous mixture into a protein-enriched condensed phase and a protein-depleted dilute phase. Protein condensates which are formed by LLPS exhibit liquid-like properties. For example, they demonstrate merging and re-rounding to minimize surface energy, and they recover rapidly after photobleaching due to fast diffusion of molecules between the phases.[1] Many proteins that undergo LLPS are either intrinsically disordered proteins (IDPs) or contain substantial intrinsically disordered regions (IDRs).[2–4] IDPs and IDRs lack defined secondary structure,[5,6] resulting in high conformational entropy and flexibility.[2,6,7] IDPs and IDRs that participate in LLPS often consist of repetitive sequences, especially those composed of polar, charged, or aromatic residues.[3] Phase separation occurs when attractive homotypic interactions between residues within disordered domains are preferred over interactions with the solvent. This preference works against entropically favored mixing, resulting in LLPS.[3] Importantly, the interactions between IDPs and IDRs that support LLPS are often weak and transient such that proteins within the condensate retain the ability to rearrange dynamically within and between the condensed and dilute phases.[7] Phase transitions occur at a range of temperatures, salt concentrations, and pH values, and depend on the specific amino acid content and sequence of the IDP or IDR.[4,8–10]

Though LLPS was first observed in the cytoplasm, it has increasingly been observed at membrane surfaces[1,11] likely due to the membrane's role as an effective substrate for locally concentrating specific proteins. Specifically, by constraining protein diffusion to two dimensions, the bilayer increases the local concentration of proteins and promotes condensate assembly. As a result, condensates form at lower concentrations on membranes than in solution.[11–13]

Membrane-bound condensates are active participants in cellular processes. For example, in T-cells, binding of extracellular ligands to the transmembrane T-cell receptor (TCR) triggers its clustering, which in turn signals intra-cellular condensation of the linker of activation T-cells protein (LAT).[14,15] Condensates of LAT then control downstream intracellular signaling kinetics.[14,15] Additionally, condensates composed of epidermal growth factor receptor (EGFR) regulate catalytic activity of SOS activation of Ras, an early activator in

---

[a] *University of Texas at Austin, Department of Biomedical Engineering, Austin, TX 78712, USA. E-mail: jcstach@austin.utexas.edu; pren@utexas.edu*

[b] *University of Texas at Austin, Department of Chemical Engineering, Austin, TX 78712, USA*

immune signaling response.[16] Condensates at the membrane also enable localized control of biochemical activity to regulate the assembly and compartmentalization of protein networks. For example, the formation of cell–cell junctions involves the sequestering of components into condensates on either side of adjacent cell membranes to drive localized assembly.[17,18] Further, early endocytic proteins Eps15 and Fcho form condensates at the membrane that recruit other components of the endocytic network.[19,20] Here the liquid nature of Fcho and Eps15 condensates in clathrin mediated endocytosis (CME) is crucial for productive pit formation and cargo internalization.[20] Similarly, liquid-like protein condensates play regulatory roles within the endoplasmic reticulum (ER) and Golgi apparatus where they are involved in cargo sorting[21,22] and promote cargo exchange between compartments.[23–25] Collectively, these findings demonstrate that condensates are not only present at membrane interfaces but also have active roles in a wide array of cellular functions. While a substantial body of knowledge exists regarding the proteins involved, there is relatively little known about their impact on the underlying lipids nor about the role the lipids themselves play in regulating LLPS at bilayers.

Recent work suggests that protein condensates and ordered lipid phases mutually reinforce one another. For example, protein condensates at the immunological synapse are more likely to form on membranes that exhibit lipid phase separation, and lipid phase separation, in turn, is more likely to occur when protein condensates are present on the membrane surface.[26] Along the same lines, membrane-bound protein condensates have been shown to locally increase lipid packing, effectively creating an ordered phase beneath them.[27] Furthermore, coupling of protein condensates across lipid bilayers has recently been observed, potentially arising from the lipid ordering induced by protein condensates at the membrane.[28]

Though available experimental data suggests a prominent role of condensates in membrane organization, the ability of experimental approaches to resolve these effects is constrained by limited spatial resolution. Molecular dynamics (MD) simulations are able to probe the detailed interactions between proteins and lipids during condensation. FUS condensates modeled with an adapted Martini 2.2 force field display phase separation dependent on the strength of protein–protein interactions.[29] A relationship between protein interaction strengths and properties of the modeled condensate, such as viscosity and droplet hydration, was also established. Additionally, simulated values are in line with experimental trends once an appropriate scaling factor was applied to modulating the protein interaction strength.[29] Recently, Martini 3 simulations of condensates of poly-lysine and poly-glutamate polymers on membrane surfaces induced curvature of charged membranes following wetting.[30] Interestingly, a bilayer of only PG charged lipids leads to complete wetting of both the positively charged poly-lysine and poly-glutamate chains. This simple system demonstrates the importance of membrane–condensate interactions in modulating condensate morphology. Another general model utilized attractive and repulsive regions in polymer chains to demonstrate that their condensates sensed curvature as a means to maximize favorable contacts upon surface wetting.[31] Recently, a model of nanoscale vesicles has revealed multiple endocytic pathways for membrane engulfment of condensates.[32]

Although simulations have advanced our understanding of condensate dynamics in bulk solution, computational studies of membrane-associated condensates lack direct experimental validation. Existing studies also have yet to systematically investigate how the balance between protein–protein and protein–lipid interactions governs the behavior of protein condensates and modulates the membrane's response. Here, we address these deficits by modeling phase separation of the RGG-rich domain of LAF1 (RGG) on membrane surfaces and directly comparing our results to experimental data. Specifically, we investigated the phase separation of RGG proteins on a bilayer using molecular dynamics simulations with the Martini 3 force field. We began by examining the impact of protein–protein interaction strength within the model, guided by an experimentally-derived temperature–concentration phase diagram. We then explored the effects of protein condensates on the physical properties of the lipids, as well as the competition between protein–protein and protein–lipid interactions. Interestingly, we found that while increasing the strength of protein–lipid interaction helps to concentrate proteins at the membrane surface, if these interactions become too strong, they can overcome attractive interactions between proteins, leading to dissolution of protein condensates, in agreement with experiments. The results of this study provide insights into the delicate balance between protein–protein and protein–lipid interactions in regulating protein condensates at the membrane surfaces.

Results and discussion

RGG proteins form a condensate on a membrane surface

To investigate phase separation of RGG proteins on a lipid bilayer, we began by placing 36 RGG individual protein chains on a 50 × 50 nm^2 POPC bilayer, with chains initially well separated, as shown in Fig. 1A, left panel. We utilized the RGG domain of LAF-1, as it is a well-studied model protein for LLPS.[33] The experimental data on membrane-bound RGG condensates to which we compare utilize Ni-NTA/histidine chemistry between N-terminal tagged proteins and functionalized lipids to bind RGG proteins to the bilayer surface.[12,28] To emulate this bond, we tethered each RGG molecule to the membrane at its N-terminus with a constant force between the center of mass of the last two residues and the center of mass of the nearest lipid head-group, as determined at $t = 0$. This force was maintained throughout the simulation. The system was then placed in a box of 50 × 50 × 20 nm^3 and solvated with water and neutralizing Cl$^-$ ions. To produce two independent simulations, we duplicated the initial coordinates and generated new particle velocities before performing equilibration. Coarse-grained methodologies have demonstrated accelerated dynamics in comparison to all-atom MD due to a smoothed potential energy landscape.[34] As a result, the dynamics observed in Martini force field simulations are accelerated by a factor of 2–10, depending on the specific system.[34,35] We report the

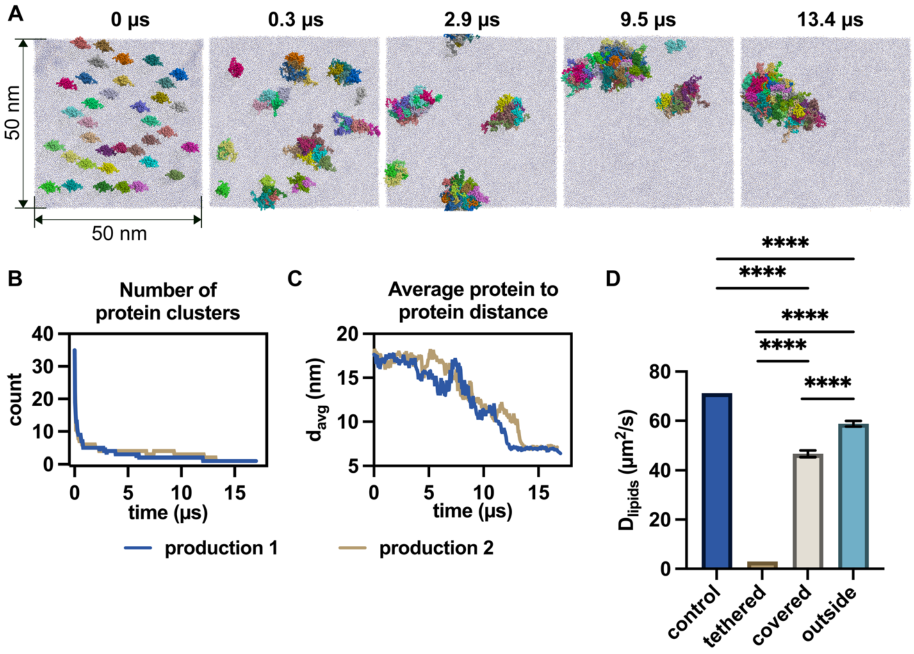

Fig. 1 RGG proteins in the simulation demonstrate merging and coarsening to form a condensate on a membrane surface. (A) Representative snapshots from a production run of 36 RGG proteins on a POPC bilayer colored by chain, viewed from above. Water and ion beads are omitted for clarity. Individual chains were placed at randomized initial positions. Clusters merged over time until a single condensate was formed. (B) The total number of protein clusters decreases as the simulation progresses. The simulation began with 36 clusters, one for each chain, and eventually coarsened to one single cluster, the condensate. The data is shown over the course of two independent production simulations. (C) The average distance between the COM of a chain to every other chain's COM over the trajectory. D_{avg} decreased over time as the proteins coarsened into a single condensate. Values are shown for two independent production simulations. (D) Diffusion constants for tethered lipids, lipids covered by the condensate, and lipids outside the condensate-covered area compared to lipids in a membrane lacking protein. Covered lipids were defined as those within a 2 nm cutoff from a protein bead. D_{lipids} is calculated from fitting the linear region of the mean square displacement of each category of lipids. The diffusion constant for covered and outside groups was averaged from 20 intervals over the period 0.5 to 10 μs, shown as mean values ± SD. All three lipid groups' diffusion was reduced compared to the control bilayer. One-sample *t*-test comparison from control to outside and covered groups and from tethered to covered and outside groups, unpaired two sample two-tailed *t*-test with Welch's correction between outside and covered groups (****$p < 0.0001$).

effective times of our simulations, noting that these differ from absolute physical times that may be observed atomistically or experimentally.

Molecular dynamics simulations were performed on this initial system for 17 μs at 300 K temperature using the Martini 3 force field. Representative images over the course of the simulation are shown in Fig. 1A, with RGG proteins colored by chain. For clarity, water and ions are not shown. The proteins were observed to self-associate into clusters over time. The clusters merged together as they diffused on the bilayer, forming progressively larger clusters (Fig. 1B). Merging occurred rapidly in the first microsecond and slowed as the clusters grew in size. This behavior was similar to that of liquid-like condensates *in vitro*, which exhibit coarsening through merging.[1] The coarsening was observed in each of the independent production simulations (Movies S1 and S2). In each simulation protein association occurred in a different order and pattern; however, both simulations ultimately converged on a single condensate comprising all 36 chains. We also tracked the average spacing, *i.e.* the pairwise distances between the centers of mass of the RGG proteins (Fig. 1C). As the condensates formed, the average distance between proteins in the system decreased until a steady state value of about 7 nm was reached, which is of the same order as experimental measurements of pore size on RGG condensates in solution.[9]

Recent work has demonstrated that the mobility of lipids beneath a membrane-bound protein condensate is reduced relative to surrounding lipids.[28] To investigate whether this effect is also present in our modeled system, we extended the production an additional 10 μs. We then calculated the 2D diffusion constant of the lipids in the system from the slope of their averaged mean square displacements. We compared the lateral diffusion constant, D_{lipids} of three groups of lipids: lipids tethered to a protein (Fig. 1D, “tethered”), lipids directly underneath the condensate (Fig. 1D, “covered”), and all other lipids outside the condensate covered area (Fig. 1D, “outside”) to lipids in a bilayer that lacked protein (Fig. 1D, “control”).

We observed that the greatest reduction in diffusion constant (95%, relative to control membrane) occurred when a lipid was directly tethered to a protein (Fig. 1D, “tethered”). Next, free lipid groups covered by the protein condensate had their diffusion reduced by over 30% in comparison to the control membrane and by 20% in comparison to the lipids outside the covered area (Fig. 1D, “covered”), possibly due to attractive forces between the lipid and protein. In comparison to the control membrane group, the lipids outside the protein covered area also demonstrated a reduction in diffusion by about 20% (Fig. 1D, "outside").

The results clearly show that covered lipids have slower diffusion on average than those outside the protein-covered area, which is in agreement with experimental data.[9]

Scaling protein–protein interactions to calibrate the simulation against experimental data

Unlike liquid-like condensates, the proteins in our initial simulations did not exchange between the condensed phase and the surrounding dilute phase. That is, rather than forming a protein-rich condensed phase surrounded by a protein-depleted dilute phase, only a condensed phase was observed once the proteins coarsened into a single cluster. This cluster was extremely stable such that once proteins joined it, they did not dissociate from it within the course of the simulation. As noted above, the Martini force field default parameters are known to overestimate protein–protein interactions, especially for disordered proteins whose high conformational entropy becomes limited by overly strong protein–protein interactions.[36,37] Therefore, when using the Martini 3 forcefield, it has been recommended to scale down the protein–protein interactions for IDRs by tuning the parameters. In other work, this has been achieved by reproducing the radius of gyration (R_g) of single RGG molecules in solution.[36] However, because protein conformation is dependent on the local environment, we performed our own calibration against experimental data in which RGG domains formed condensates on the surfaces of planar suspended membranes[28] (Fig. 2). Specifically, in the experiments, the relative fluorescence intensities of the protein-rich and protein-depleted phases were measured at each temperature, providing a rough estimate of the relative protein concentration in each phase (Fig. 2B). Using this approach, the relative protein density in the condensed protein-rich phase decreased as the system was heated (Fig. 2D, black, left). Concurrently, the relative protein density of the protein-depleted phase increased (Fig. 2D, black, right). Notably, because fluorescence intensity is quantified relative to background signal, the measurements are subject to significant noise, especially for the relatively dim protein-dilute phase (Fig. 2A). Nonetheless, these data demonstrate that the protein-dense phase should become significantly less dense with increasing temperature.

We sought to adjust the scaling of our model to emulate these data. Non-bonded interactions in the Martini force field are represented using a Lennard-Jones potential, to which we added a linear scaling factor, "α", to all protein beads, excluding bead types used to represent water, ions, and the lipids in our system. We followed a similar approach to Benayad *et al.*, who compared excess transfer free energy of a protein between the dilute phase and condensed phase in their simulation to experimentally obtained values to obtain a scaling factor.[29] We adapted the slab morphology, often used to examine phase transitions in three-dimensions, to a two-dimensional

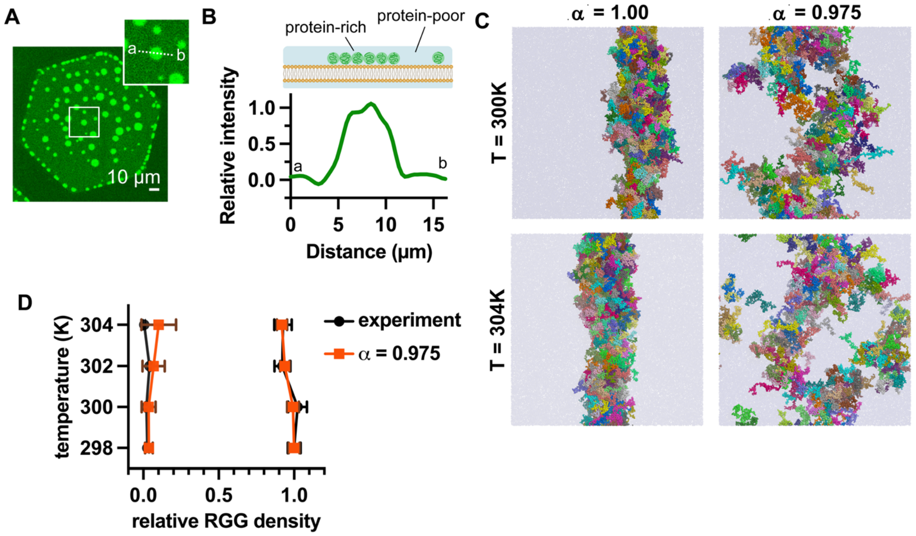

Fig. 2 Scaling protein–protein interactions to calibrate the simulation against experimental data. (A) Representative microscopic image of a hexagonal membrane showing protein-rich (brighter) and protein-poor (dimmer) phases formed by fluorescently labeled RGG proteins. (B) (Top) Cartoon of a membrane cross-section. (Bottom) Relative intensity profile along the dotted line in (A) (from a to b), where regions with relative intensity of 0 and 1 correspond to protein-poor and protein-rich phases, respectively. Relative intensity (I_R) was defined as $I_R = (I - I_D)/(I_B - I_D)$, where I, I_D, and I_B indicate the fluorescence intensity of the region of interest, the intensity of the dimmer region, and the intensity of the brighter region, respectively. (C) Representative images from production simulations of 120 RGG chain slabs at 300 K and 304 K for scaling factors $\alpha = 1.00$ and $\alpha = 0.975$, viewed from above. Without scaling, the slab remained tightly packed and did not respond to temperature ($\alpha = 1.00$, left). Reduced protein–protein interactions resulted in temperature-driven expansion of the slab ($\alpha = 0.975$, right). (D) Phase diagram of protein expansion from *in vitro* melting experiment of RGG condensates (black) and $\alpha = 0.975$ scaled slab simulation (orange). Scaling by a factor of 0.975 created a phase diagram in close agreement with experimentally measured phase behavior. For slab simulations, data points are shown as mean values ± SD from $n = 3$ for 298 K, 300 K, and 302 K, $n = 2$ for 304 K. For experiments, data points are shown as mean values ± SD from analyzing 3–10 protein-rich and protein-poor regions from three independent experiments at each temperature.

membrane by assembling a strip of RGG protein chains, which, due to the periodicity of our boundary conditions, is effectively infinite. The slab consisted of 120 RGG chains, tethered as previously described, on a 50 × 50 nm^2 POPC bilayer. Production was performed for 10 μs, or until system convergence as evaluated by condensed phase density.

We first examined the slab without scaling protein interactions, $\alpha = 1.00$. At 300 K, the protein slab remained fully intact throughout the trajectory (Fig. 2C, left, top and Movie S3). No proteins were observed outside of the main protein condensate. Using the same initial coordinates, the simulation was then performed at 304 K (Fig. 2C, left, bottom). The proteins were observed to reside exclusively in the slab. Additionally, the slab did not exhibit temperature-driven expansion, behavior which is indicative of overly strong intermolecular interactions. As noted above, this observation aligns with prior reports highlighting the tendency of the Martini force field to overestimate interaction strengths, particularly for IDPs.[29,36] Next, the simulations were repeated with reduced protein–protein interaction by a factor of 0.975. At 300 K, the condensate expanded over a greater area than its unscaled counterpart (Fig. 2C, right, top). Moreover, several individual chains were able to overcome the thermodynamic barrier to dissociate from the slab and sample the surrounding membrane region (Movie S4). As a result, we observed the coexistence of a condensed and dilute phase. When the temperature of the $\alpha = 0.975$ system was raised to 304 K, the slab expanded further (Fig. 2C, right, bottom) and more chains dissociated into the dilute phase. Based on these observations, it was evident that reducing protein–protein interaction strength improved the condensate's responsiveness to temperature, yielding phase behavior more consistent with experimental expectations.

We next sought to determine which scaling value provided the best match to the experimental data described above. For this purpose, additional simulations were performed over a range of temperatures to construct a phase diagram for comparison to the phase diagram extracted from experiments. The slope of the condensed-phase density profile (Fig. 2D, right) reflects the thermal expansion behavior of the condensate. The separation between the condensed and dilute phase boundaries represents the relative protein partitioning between the two phases. Densities from our simulations were calculated by counting the total number protein beads in each phase and dividing by the corresponding two-dimensional area. The values were then normalized to the density at 298 K.

In our scaled slab system for $\alpha = 0.975$, we observed that the relative partitioning between the condensed and dilute protein phases decreased with increasing system temperature (Fig. 2D, orange), in agreement with the experimental data. Incremental increases in temperature led to a progressive decrease in condensed-phase density (Fig. 2D, orange, right), corresponding to greater occupancy in the dilute phase (Fig. 2D, orange, left). For further validation of this α value, we compared the change in relative partitioning at values greater and less than 0.975 (Fig. S1). At $\alpha = 0.98$, the resultant condensed phase boundary was nearly vertical, indicating insufficient scaling (Fig. S1B and C). Lowering α to 0.9725 did not improve the slope of expansion (Fig. S1C), and the absolute density was reduced to a nearly melted state, even at 300 K (Fig. S1B). Thus, we concluded that, within our modeling framework, 0.975 was the most appropriate scaling factor for further exploration of our condensate-bilayer systems.

Introducing charged lipids increased condensate wetting of the bilayer

Next, we explored the effect of protein–lipid interactions on the assembly of protein condensates at membrane surfaces. Specifically, we added negatively charged lipids to the bilayer to promote electrostatic interactions with charged residues with RGG. RGG contains 48 charged residues, half of which are positively charged arginines. POPC (PC) lipids have a net neutrally charged head group consisting of a −1 charged phosphate and positive +1 ammonium. POPS (PS) lipids instead consist of a −1 phosphate and neutral L-serine group, such that the net charge per lipid is −1.

We began our investigation without scaling protein–protein interactions ($\alpha = 1$). We utilized a pre-formed condensate taken from the unscaled coarsening simulations in Fig. 1 to initialize our system. We then replaced PC lipids in the bilayer with negatively charged PS lipids in increasing fractions of 0 (no PS), 0.1, 0.3, and 0.5 at $t = 0$. We ran the simulations for 10 μs each, monitoring the radius of gyration of the condensate for system convergence.

For this unscaled system, we observed increased wetting of the condensates on the bilayer when negatively charged lipids were introduced (Fig. 3A). First, we observed the condensate without charge in the bilayer was rounded and compact (Fig. 3A, first panel and Movie S5). Initially, the shape of the condensate responded relatively little to the addition of PS in 0.1 and 0.3 fractions (Fig. 3A, second and third panels). However, with the addition of PS in 0.5 fraction, the condensate flattened as its contact with the membrane surface significantly expanded (Fig. 3A, fourth panel and Movie S6). In order to quantify the expansion of the condensate in the *xy* plane, we calculated the mean radial distance of a protein particle to the condensate's *z*-axis center of mass (R_{avg}) during the final 2 μs of each trajectory (Fig. 3B). The radial distance between a given particle and the condensate's center of mass can range from zero for proteins located at the center of mass to a maximum value corresponding to the outer radius of the mass distribution. Assuming uniform particle density within the condensate, the mean radial distance should be slightly greater than half the condensate radius, reflecting the geometrical capacity to accommodate more particles at larger radii. The mass distribution R_{avg} grew progressively as the fraction of PS lipids in the bilayer was increased. With the addition of 0.1 PS, R_{avg} increased by a third of a nanometer (or 7%), while the addition of 0.3 PS further elevated this difference to a half nanometer difference (or 9%) relative to the 0 PS condition. The addition of 0.5 PS resulted in the largest shift in the average radial distance, which increased by ~1.2 nm, a 20% difference over the neutral bilayer.

This enhanced wetting behavior was further explored by quantifying the average number of lipid contacts over all

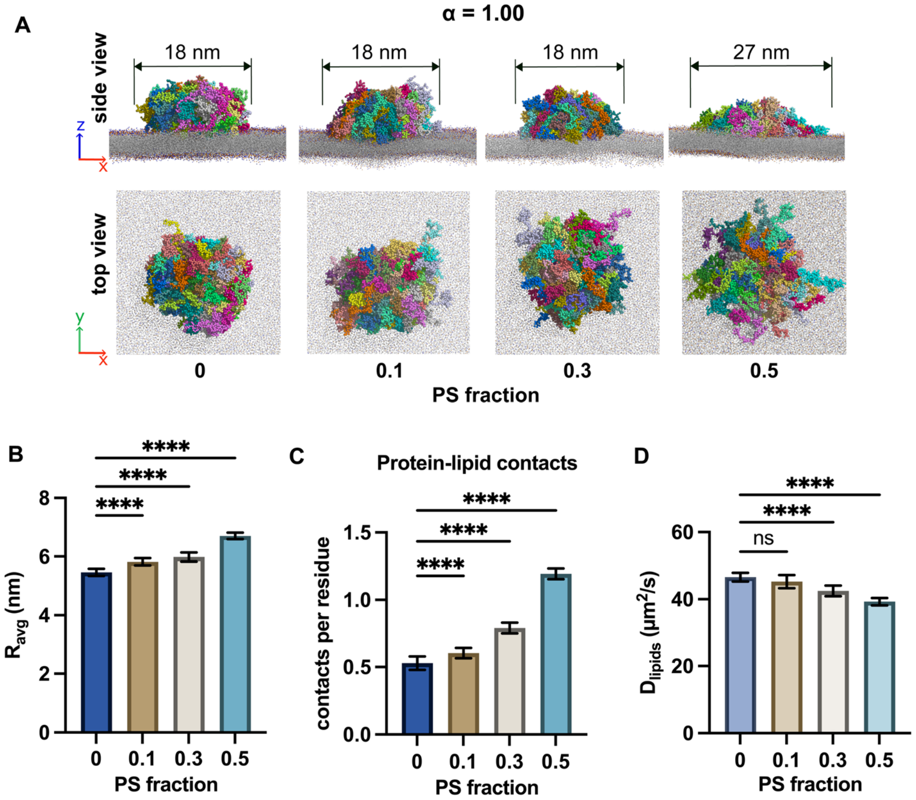

Fig. 3 Introducing charged lipids increased condensate wetting of the bilayer. (A) Snapshots from productions of the condensate on increasing PS lipid fractions as side view (top row) and from above (bottom row). The condensate diameter is also labeled. A visible change in condensate morphology occurred when the PS fraction was increased to 0.5. (B) Radius of gyration in the *xy* plane (R_{avg}). Calculated as the average distance of a protein particle to the overall protein *z*-axis center of mass as a measure of condensate spread on the bilayer. Distance to the condensate center increased with more charge in the bilayer. (C) Number of protein–lipid contacts per residue for different PS lipid fractions averaged across 20 frames over the final 2 μs. Protein–lipid contacts were defined as a residue center of mass within 10 Å of a lipid headgroup particle. Protein–lipid contacts more than doubled when PS content was raised to 0.5 and increased about 50% when PS content was 0.3. (D) Diffusion constant for covered lipids in systems of varied PS lipid fraction. Diffusion trended downwards as the PS fraction was increased. Data for (B and C) were averaged over 20 frames in the final 2 μs. Diffusion was averaged from 20 intervals over the period 0.5 to 10 μs. Data shown as mean values ± SD. Comparisons are unpaired two-tailed *t*-tests with Welch's correction (*****p* < 0.0001).

protein residues in the last 2 μs of the trajectories (Fig. 3C). The number of protein lipid contacts did not substantially increase with the addition of 0.1 PS (Fig. 3C, brown), suggesting that the electrostatic contribution at this fraction was insufficient to promote additional wetting. In contrast, the addition of 0.3 PS to the bilayer resulted in a nearly 50% increase in protein–lipid contacts compared to a neutral bilayer (Fig. 3C, grey). Furthermore, the addition of a 0.5 PS fraction more than doubled the occurrence of protein–lipid contact (Fig. 3C, teal).

Next we investigated the effect of increased affinity on the behavior of the underlying lipids. Here, we focused on the diffusivity of the lipids which were directly wet by the protein condensate, previously named the "covered" lipid group (Fig. 1D). Lipids in a bilayer with 0.1 fraction PS did not demonstrate a statistically significant shift in mobility compared to a neutral bilayer (Fig. 3D, brown). Increasing to a 0.3 PS fraction resulted in a reduction in diffusion coefficient by approximately 9% relative to the neutral bilayer (Fig. 3D, grey). The increase to 0.5 PS resulted in a 15% reduction in lipid diffusivity compared to the neutral bilayer (Fig. 3D, teal). These data suggest that lipid diffusion slowed down as the electrostatic attraction between lipids and proteins increased. More broadly, these results suggest that the addition of a sufficient fraction of charged lipids to the bilayer increased the mutual affinity between the RGG condensate and membrane surface. Despite the addition of an electrostatic contribution to protein–lipid interaction, the overall system dynamics were still primarily driven by dominant protein–protein interactions when unscaled. Therefore, we next examine the impact of scaling ($\alpha < 1$) on the balance between protein–lipid and protein–protein interactions.

The addition of charged lipids opposed condensation on the membrane when protein–protein interactions were scaled

Next, we explored the system using the previously determined scaling parameter of $\alpha = 0.975$ applied to the nonbonded interactions between all protein beads. No charge–charge interactions were modified. As with the unscaled 36 RGG systems in Fig. 3, we used the final coordinates of the coarsening production as our initial configuration. As in the previous section, at $t = 0$ we substituted PC lipids in the bilayer for PS lipids in fractions of 0 (no PS), 0.1, 0.3, and 0.5. Simultaneously, we applied the scaling factor $\alpha = 0.975$ to the protein–protein interactions. Each simulation was then run for 10 μs.

In the absence of charged lipids in the bilayer, individual chains were observed to disassociate from the condensate and sample the dilute phase (Fig. 4A, first panel), as expected based on the results of our slab simulations. Importantly, this behavior is in contrast to the unscaled condensate system, which remained dense and showed no dissociation activity. Increasing the PS fraction to 0.1 yielded no obvious difference in condensate morphology over the neutral membrane (Fig. 4A, second panel and Movie S7). At a higher PS fraction of 0.3, we observed more protein chains diffusing outside of the main condensate (Fig. 4A, third panel). In addition, the condensate exhibited expansion in the *xy* plane, while flattening in the *z* dimension. Even with this expansion, defined dilute and condensed phases remained observable throughout the duration of the trajectory (Movie S8). However, upon the addition of 0.5 PS, phase separation was no longer observed and the condensate appeared to melt such that individual chains and

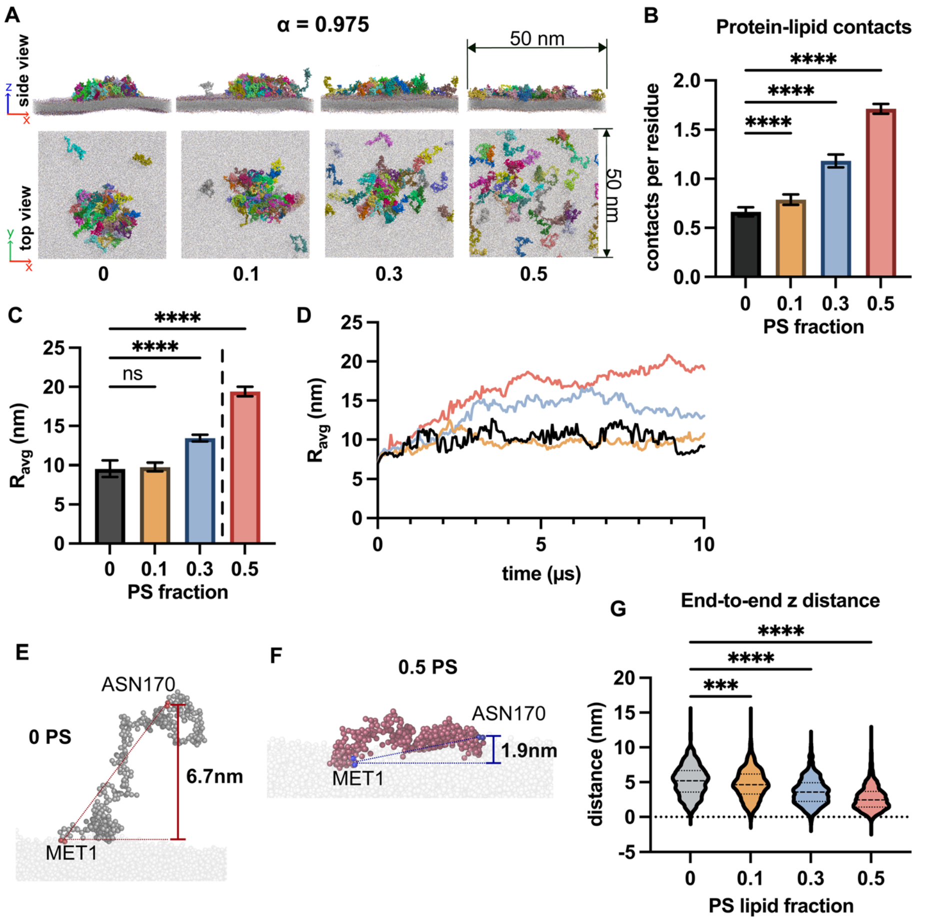

Fig. 4 The addition of charged lipids opposed condensation on the membrane when protein–protein interactions were scaled. (A) Snapshots from simulations of 36 RGG chains on bilayers of increasing PS lipid fractions. The protein–protein interactions were scaled by $\alpha = 0.975$. The proteins were completely dispersed at 0.5 PS. At 0.3 PS, the condensate was loosely held together with several proteins in the dilute phase. Condensates were well-formed with PS fractions of 0 and 0.1. (B) Number of protein–lipid contacts per residue for different PS lipid fractions averaged across 20 frames over the final 2 μs. Contacts between protein residues and lipid headgroups increased with charge fraction. Reduced protein–protein interaction strengths resulted in a greater number of contacts in comparison to their unscaled counterparts (Fig. 3). (C) Average distance of a protein particle to the overall protein *z*-axis center of mass (R_{avg}) as a measure of condensate spread on the bilayer. Introducing charged lipids increases protein mass distribution. The average distance of a protein particle to the total protein COM (R_{avg}), nearly doubled from 0 PS to 0.5 PS in the bilayer. A dashed line indicates the PS fraction beyond which the condensate was no longer defined. (D) R_{avg} over the course of the trajectory. Protein expansion occurred over the first half of the trajectory for fractions 0.3 and 0.5 before reaching a steady state. (E) Representative protein conformation from condensate on 0 PS membrane with labeled *z* distance between terminal residues (6.7 nm). The protein chain was within the main droplet seen in (A). Methionine (MET1) is tethered to the bilayer while final asparagine (ASN170) is free. (F) Representative protein conformation from condensate on 0.5 PS membrane with labeled *z* distance between terminal residues (1.9 nm). The chain shown was unassociated with other proteins at this moment. (G) Violin plot summary of end-to-end distances between terminal residues for PS fractions. Distances were measured for each of 36 RGG chains over 20 frames in 2 μs ($n = 720$). Data for (B and C) were averaged over 20 frames in the final 2 μs. Data are shown as mean values ± SD. Comparisons are unpaired two-tailed *t*-tests with Welch's correction (***$p < 0.001$, ****$p < 0.0001$).

small, short-lived clusters diffused throughout the membrane surface (Fig. 4A, third panel and Movie S9).

In the conditions of 0.3 and 0.5 PS fractions, proteins appeared to forgo homotypic interactions in favor of protein–lipid interactions. In order to further explore the degree to which charge influences protein–lipid interaction, we quantified the number of lipid contacts per residue (Fig. 4B). Minimal changes in protein–lipid interaction frequency were observed upon increasing the charged lipid fraction to 0.1 PS. However, incorporation of 0.3 PS resulted in more than a twofold increase in protein–lipid contacts while preserving a well-defined condensed phase. At 0.5 PS fraction, the frequency of protein–lipid contacts increased over threefold relative to the neutral condition, though interestingly, this effect occurred alongside the loss of a defined condensed phase.

We also repeated analysis of the R_{avg} (Fig. 4C) and how it changed over time (Fig. 4D). The mass distribution was elevated compared to the unscaled systems, due to condensate expansion and addition of chains in the dilute phase (Fig. 4C). Compared to the neutral bilayer, adding 0.1 PS resulted in no significant difference. We also observed that the R_{avg} in the 0 PS and 0.1 PS conditions remained constant over the course of the trajectory (Fig. 4D, black and yellow), further demonstrating the favorability of being in the condensate over the dilute phase. In contrast, when charge was increased to 0.3 PS, proteins occupied 20% more space on the bilayer compared to the lower PS fractions (Fig. 4C, blue). Further increase to 0.5 PS roughly doubled the mass distribution on the bilayer (Fig. 4C, red). The expansion of the condensates on 0.3 and 0.5 PS fraction bilayers occurred over the first half of the trajectory until a steady state was reached (Fig. 4D, blue and red). It appeared that the inclusion of charged lipids not only opposed condensate formation but was also able to actively disassemble pre-existing condensates.

Analysis of individual RGG protein chains revealed a distinct shift in orientation under higher charge conditions, relative to those sampling the dilute phase in systems with lower charged lipid content (Fig. 4E–G). In the absence of charged lipids, protein chains primarily interact with neighboring proteins and the solvent, adopting an extended, upright conformation perpendicular to the membrane surface (Fig. 4E). In the presence of a 0.5 PS lipid fraction, proteins were oriented closer to the membrane and are almost horizontal (Fig. 4F). We quantified the *z*-distance between the membrane-tethered N-terminal and free C-terminal residues of each protein, as labeled in Fig. 4E and F (Fig. 4G). This end-to-end distance was recorded over the last two microseconds of each PS fraction simulation. Negative values, where the C-terminus is below the N-terminus, were observed for all PS fractions due to bilayer fluctuations that induced local negative curvature. Increasing the PS fraction from 0 PS to 0.5 PS resulted in a progressive decrease in the distribution of *z*-distances upon the addition of 0.1 PS (8%, Fig. 4G, yellow), 0.3 PS (~30%, Fig. 4G, blue) and 0.5 PS (~50%, Fig. 4G, red). This trend supports observations from Fig. 4A, indicating that increased bilayer charge induces a reorientation of the protein chains. This effect is likely driven by extension of the chains as they maximize their interaction with charged membrane lipids, Fig. 4E and F. The implication of these data is that charge in the membrane can act in opposition to condensate formation. In conditions with insufficient membrane charge, it was most favorable for proteins to remain in the condensate and interact with each other. In contrast, attractive electrostatic interactions with charged lipids provided a favorable alternative to the protein–protein interactions in the condensate, reflected in increased protein–lipid contacts and dissolution of the condensate (Fig. 4B). If increased association between proteins and anionic lipids opposes phase separation, could removing the tether between proteins and membranes strengthen phase separation? Our next series of simulations sought to address this question.

Charged lipids keep protein condensates on the membrane in the absence of a tethering constraint

Thus far, protein chains were subjected to a constant-force tether anchoring them strongly to the bilayer, thereby constraining their motion and conformational flexibility. We now examine how condensate behavior changes in the absence of this constraint. Though several *in vitro* studies have used tethering to keep condensates at the bilayer,[12,26,28] membrane-associated condensates do not necessarily contain transmembrane domains or other structured lipid binding.[38,39] We therefore sought additional insight on how disordered protein condensates interacted with the bilayer in the absence of a strong membrane binding component. Results in Fig. 4 showed that tethering promoted protein association with charged lipids, contributing to condensate disassembly. Based on these findings, we hypothesized that removal of the tether could shift the balance of protein–protein and protein–lipid interactions to more strongly favor the condensed phase relative to the tethered condition.

As before, we use the coordinates from the pre-formed 36 RGG condensate system as the initial configuration. At $t = 0$, we replaced PC lipids in the bilayer with PS lipids in increasing fractions of 0 (no charge), 0.1, 0.3 and 0.5 and simultaneously removed the tethering force.

First, we examined the system without scaling the protein–protein interactions ($\alpha = 0$, Fig. S2). At 0 PS, the condensate gradually lost contact with the bilayer until it was fully dissociated from the surface in the last microsecond (Fig. S2A). A PS fraction of 0.1 did not fully recover the contact observed with the tether. In contrast, a PS fraction of 0.3 recovered the condensate's contact with the bilayer for the duration of the trajectory. Further increasing to 0.5 PS, we observed increased wetting. The distribution of the proteins was reduced compared to the tethered case, also indicating more rounded condensates (Fig. S2B). The difference in R_{avg} was not as pronounced as in the tethered case, indicating that condensate morphology in these unscaled systems is dominated by the strong protein–protein interactions. However, we observed fewer protein lipid contacts in the untethered systems compared to their tethered counterparts: ~80% fewer for 0 and 0.1 PS conditions, ~40% fewer for 0.3 PS, and ~20% fewer for 0.5 PS (Fig. S2C and 3C). Within the untethered condition, increasing the PS fraction from 0 to 0.5 resulted in an ∼8-fold increase in contacts, and a ∼4-fold increase from 0 to 0.3 (Fig. S2C). The number of lipid contacts per amino acid more than doubled between the 0.3 and 0.5 PS fractions and were reduced to nearly zero at 0.1 and 0 PS. Similarly to the tethered case, the diffusion of the covered lipids was more dampened at higher charge fractions (Fig. S2D). Overall, when a substantial fraction of lipid head groups were changed to POPS, condensates composed of RGG remained attached to membrane surfaces in the absence of tethering.

We next repeated the simulations with α scaled to 0.975 and tethering constraints removed at $t = 0$. Here, for PS fractions of 0 and 0.1, the condensate expanded isotropically in three dimensions, occupying a larger volume in solution (Fig. 5A). At higher PS fractions (0.3 and 0.5), expansion was instead confined predominantly to the *xy*-plane (Fig. 5A), indicating enhanced membrane association that opposed vertical expansion. However, under these conditions, proteins disassociated from the condensate and bilayer into a dilute phase in solution. Under the 0.5 PS condition, those proteins that remained attached to the membrane surface occupied a single dilute phase. These changes were reflected in a reduction in the number of protein–lipid contacts (Fig. 5B) relative to the tethered systems (Fig. 4B) for all PS fractions, a consequence of both weakened protein–protein interactions due to scaling and diminished membrane association following the removal of the tether.

The inclusion of charged lipids in the membrane opposed condensate formation when the tether was removed. As the condensed phase disassembled, R_{avg} increased by 2 and 3 fold as the PS fraction increased from 0 to 0.3 and 0.5, respectively (Fig. 5C). The disassembly of the condensates on 0.3 and 0.5 PS bilayers continued to occur in the second half of the trajectory, after $t = 5$ μs (Fig. 4D). The untethered condensate at 0.3 PS had fewer proteins in the dilute phase than the same system with

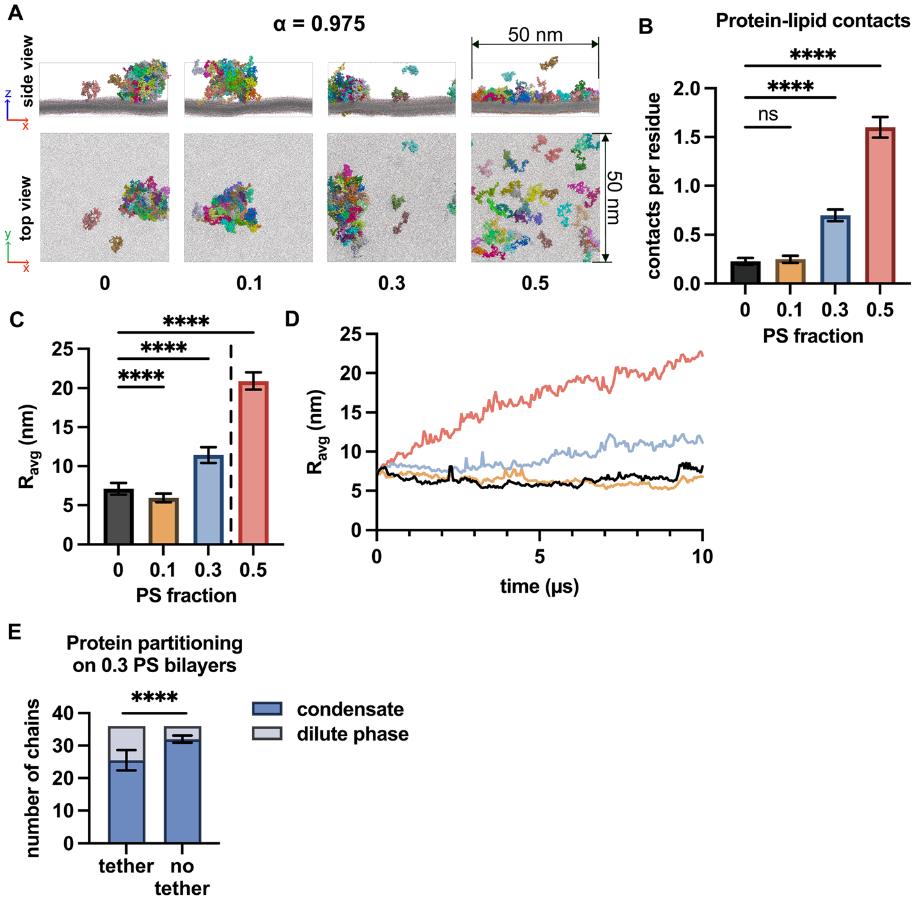

Fig. 5 Charged lipids keep protein condensates on the membrane in the absence of a tethering constraint. (A) Snapshots from the ends of trajectories, with the protein tether removed at $t = 0$. The fraction of PS lipids increases from left to right. The condensate expanded to fill space in *z*-dimension in both 0 and 0.1 PS cases. In the 0.3 PS case, the condensate remained close to the bilayer, but several proteins escaped into bulk solution or a membrane-bound dilute phase. The 0.5 PS fraction condensate disassembled onto the bilayer, with several proteins escaping to solution. (B) Number of lipid contacts per residue averaged over 20 frames in the final 2 μs. (C) Comparison of R_{avg} around the *z* axis for different PS lipid fractions. Condensate dissolution at high charged lipid fraction promoted spreading in the *xy* plane. A dashed line indicates the PS fraction beyond which the condensate was no longer defined. (D) Trajectory of R_{avg} for each PS fraction, colored as in (C). Spreading occurred over the entire trajectory for the upper two PS lipid fractions but was stable for 0 and 0.1 PS. (E) Partitioning of the 36 RGG chains between the condensate (dark blue) and the dilute phase, either membrane-bound or in solution, (light grey) in systems with 0.3 PS in the bilayer. Comparison between partitioning when proteins are tethered (left) and when tethering is removed (right). Statistics: values for (B, C, and E) were averaged over 20 frames in the final 2 μs. Data are shown as mean values ± SD. Unpaired *t*-tests with Welch's correction (*****p* < 0.0001).

protein tethering (Fig. 3A, third panel and Fig. 4A, third panel). We quantified protein distribution between the primary condensate and the dilute phase, both attached to the membrane and in solution, during the final 2 μs for both tethered and untethered conditions (Fig. 4E). On average, there were ~20% more chains in the primary condensate, and 60% fewer in the dilute phase, when tethering was removed, suggesting that the tethering acted as a promoter of disassembly.

In experiments, adding charged lipids to the membrane reduces the density of RGG proteins in the condensed phase

We next compared our predictions to experimental data. Specifically, we tested the prediction that introducing charge to the bilayer would oppose condensate formation. We created suspended planar lipid membranes within the hexagonal holes of transmission electron microscopy (TEM) grids, as described previously.[28,40] Each grid contained 150 holes, each with a diameter of approximately 150 μm, enabling visualization of multiple independent membrane surfaces per field of view using fluorescence confocal microscopy (Fig. 6A). We added C-terminal histidine-tagged RGG (His-RGG), labeled with Atto 488, to planar membranes at a concentration of 1 μM, which is more than 10 times lower than the concentration required for the phase separation of RGG in solution.[22,33] Here, binding of His-RGG to the membrane was achieved through interactions between histidine and Ni-NTA. All membranes contained 15 mol% DGS-Ni-NTA lipids for this purpose. The remainder of the lipids in the membrane were either purely DOPC (85 mol%) or a mixture of DOPC (65 mol%) and the negatively charged lipid DOPS (20 mol%). Upon addition of His-RGG to these membranes, the fluorescence intensity of membrane-bound RGG was homogeneous over the surface of the membrane, indicating uniform protein binding. However, co-existing brighter and dimmer phases began to emerge after a few

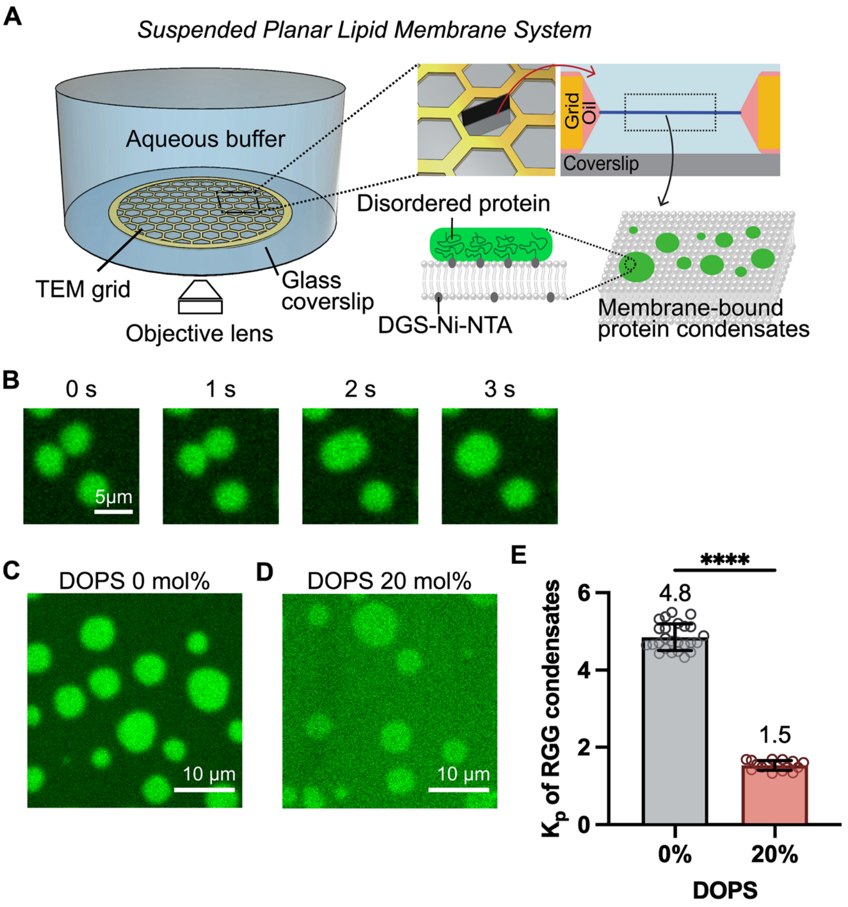

Fig. 6 In experiments, adding charged lipids to the membrane reduces the density of RGG proteins in the condensed phase. (A) Schematic of the suspended planar membrane system where suspended membranes span each hexagonal hole of a transmission electron microscopy (TEM) grid. Histidine-tagged proteins with disordered regions, in this case, RGG, bind to the membrane through histidine–nickel interactions and form protein condensates *via* spontaneous protein phase separation. (B) Merging and re-rounding of membrane-bound RGG condensates. (C and D) Representative microscopic images of RGG condensates on the membrane. Membrane composition for (C): 85 mol% DOPC, 15 mol% DGS-Ni-NTA. Membrane composition for (D): 65 mol% DOPC, 20 mol% DOPS, 15 mol% DGS-Ni-NTA. (E) Partition coefficient (K_P) of RGG proteins for each membrane composition. K_P was defined as $K_P = I_B/I_D$, where I_B and I_D indicate the fluorescence intensity of the brighter (condensate) and the dimmer regions in the image after subtracting the background intensity, respectively. Buffer: 25 mM HEPES, 100 mM NaCl, pH 7.4. 1 μM of His-RGG labeled with Atto 488 was used. Unpaired two-tailed *t*-test with Welch's correction (*****p* < 0.0001).

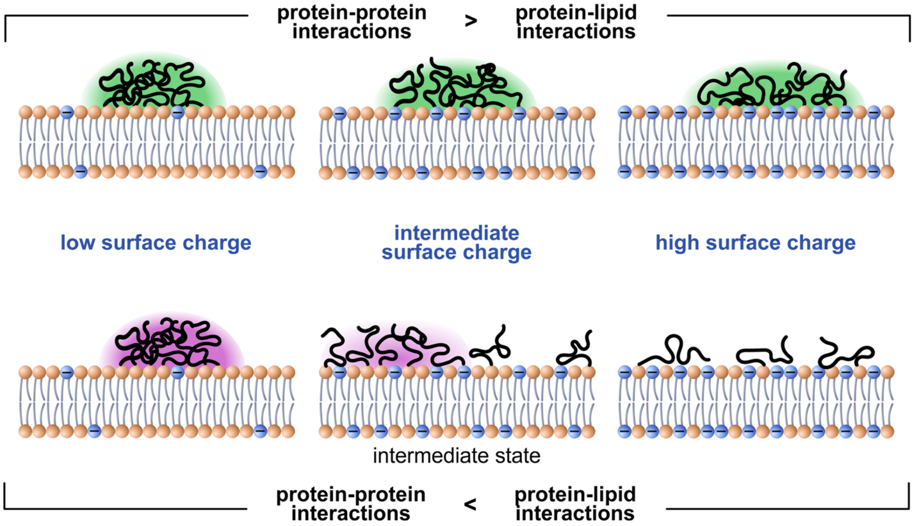

Fig. 7 Surface charge regulates membrane-associated protein condensation. Condensates characterized by a strong protein–protein interaction network are stabilized on the membrane by increased protein–lipid interactions from surface charge (top). Surface charge disrupts condensate formation when protein–protein interactions are weakened in comparison to protein–lipid interactions (bottom).

minutes, indicating phase separation of the membrane-bound RGG protein into protein-rich (brighter) and protein-depleted (dimmer) phases on the membrane surface (Fig. 6B–D). The protein-rich condensates on the membrane exhibited round shapes, merging and re-rounding upon contact, indicative of LLPS (Fig. 6B).

We estimated the relative partitioning (K_P) between the protein-rich condensed phase and protein-depleted continuous phase as a ratio between their fluorescence intensities (Fig. 6E). On the neutral membrane, K_P was approximately 5. In contrast, with the addition of negatively charged DOPS lipids (20 mol%), K_P decreased to 1.5. The reduced partitioning between the two phases upon addition of DOPS mirrors the results of our simulations (Fig. 4A and E) and suggests that as protein–lipid interactions become stronger, they compete with protein–protein interactions resulting in a lower density of proteins within the condensed phase.

Conclusions

Phase separation of proteins on membrane surfaces is being observed in an increasing number of diverse biological contexts.[11] Recent experiments suggest that protein condensates locally organize lipids.[27,28] However, the detailed mechanisms by which proteins and lipids interact to create membrane-bound condensates remain largely unknown due to experimental limitations. To gain a molecular level insight to condensate–membrane systems, we utilized coarse-grained molecular dynamics simulations to model phase separation of RGG proteins on membrane bilayers.

We began by attaching RGG proteins to a bilayer, which coarsened over time to form membrane-bound protein condensates. However, the resulting condensates failed to exhibit dynamic exchange of proteins between the condensed phase and its surroundings, a hallmark of LLPS. We therefore applied a scaling parameter α to protein–protein interactions to reproduce thermal expansion of RGG condensates observed in experiments.

Next, we utilized this scaling to study RGG condensates on bilayers containing charge. Without scaling protein–protein interactions, the addition of charge resulted in increased wetting of the membrane by the condensate. Once the scaling was applied, we observed that at low charged lipid concentrations, the proteins existed in clearly defined condensed and dilute phases. However, above a critical concentration of charged lipids, we observed the dissolution of the condensate on the membrane, suggesting that protein–lipid interacts outcompeted protein–protein interactions. Condensates investigated using an *in vitro* model demonstrated similar behavior, where partitioning between the condensed and dilute phases was reduced in the presence of charged lipids. Furthermore, our results showed that charged lipids can sustain protein–membrane interactions without a tethering force. Intriguingly, removal of the tether promoted greater protein partitioning to the condensate in the presence of charged lipids, suggesting that reducing the strength of protein attachment to membranes can promote protein phase separation.

Though several studies have established that association of proteins to membranes promotes the assembly of condensates,[13,20,26] our results indicate that the opposite is also true: the bilayer can work against the formation of protein condensates when protein–lipid interactions compete with protein–protein interactions. While this observation can be explained by principles of physical chemistry, our work is the first to observe it directly, both computationally and experimentally. More broadly, our observations suggest that whether the membrane acts as a promoter or competitor of condensate formation is dependent on the specific balance between protein–protein and protein–lipid interactions. From a biological perspective, our results suggest a more complex picture of condensate regulation by membranes than previously proposed, where changes in membrane charge and composition, orchestrated by cellular enzymes and metabolic pathways, may regulate the dynamic assembly and disassembly of protein condensates. We propose that surface charge can serve as an effective regulatory mechanism of membrane-associated condensation in dynamic processes, extending beyond its role in protein recruitment. Charged lipids may stabilize condensate association with the bilayer, evidenced by increased wetting and a resulting change in lipid diffusion (Fig. 7, top). Alternatively, if the strength of protein–protein interactions is reduced in comparison to protein–lipid interactions, charge may disrupt condensate formation, as in the high PS fraction condition (Fig. 7, bottom). In this way, surface charge provides a potential means of controlling the composition and identity of condensates at the membrane.

Though not explored in this work, ionic strength has also been shown to affect condensate stability. For RGG, whose phase separation is primarily driven by charge–charge interactions, screening results in the salting out, or destabilization, of condensates. Varying salt concentration introduces an additional dimension to the parameter space, which includes α to tune protein–protein interactions, and the fraction of charged lipids. Future study may expand on how ionic strength modulates membrane-associated condensation in the presence of charged lipid species.

Methods

Simulation methods

The Martini 3.0 force field[34,41] and GROMACS[42,43] engine were used for all MD simulations. Structures and trajectories were visualized using pymol.[44] The initial all-atom structure for the protein was taken from an AlphaFold[45] structure prediction of the 170 residue sequence of RGG. This structure was then coarse grained using *martinize2*[46] and solvated using *insane*.[47] Short minimization, equilibration, and production simulations were then performed using the recommended CHARMM-GUI[48,49] parameters to obtain a more compact conformation for membrane tethering. We assembled a 50 × 50 nm^2 bilayer in CHARMM-GUI. Then, proteins were added in the desired conformation and the protein–membrane system was solvated with water and 100 mM NaCl using *insane*.

Tethering. We attached proteins to the bilayer using a constant force pull-coordinate between the center of mass of the terminal two residues of each chain and the nearest lipid headgroup. This force was maintained throughout equilibration and production. Pull code samples are provided as mdp files in SI.

Calculation of diffusion coefficient. Covered and outside lipid groups were redefined at periodic intervals throughout the simulation. This interval length was determined by dividing the condensate area by the diffusion constant of the control lipid group as an estimate of the time it would take for a lipid to explore the space. To calculate the lateral diffusion of covered and outside lipid groups, we used the GROMACS tool gmx msd for the molecules in the group, which uses linear regression to fit a slope to the molecules' mean square displacement and obtain the 2-dimensional constant D_{lipids}. The diffusion constant is shown as an average of twenty windows over the simulation, with standard deviation representing variation between windows. For tethered and control lipid groups, we applied the analysis over the whole trajectory.

Small droplet and charged bilayer simulations. We used the final configuration of the initial coarsening production MD (Fig. 1) as the starting conformation for small droplet experiments. Charge was introduced replacing the specified fraction of POPC lipids with POPS lipids at random locations in both leaflets in the bilayer for even distribution. Untethered production runs have the constant tethering force removed at $t = 0$ before production. Minimization and equilibration were performed using the recommended protocol from CHARMM-GUI. Production was performed in the *NPT* ensemble with C-rescale barostat and semi-isotropic coupling at a pressure of 1 bar in the z dimension and 1 bar in the xy plane. The systems were run for 10 μs each. Initial conformation states, equilibration parameters and production parameters are provided in SI.

Scaling and slab simulations. The MARTINI force field uses a Lennard-Jones potential to describe non-bonded van der Waals interactions. In order to control protein–protein interaction strengths, we added a general scaling factor α, to the default parameters:

$$V(r) = 4\varepsilon_{ij}\alpha\left[\left(\frac{\sigma}{r}\right)^{12} - \left(\frac{\sigma}{r}\right)^{12}\right]$$

We excluded bead types used to describe lipids, water, and salt. Slab experiments were run with slight tension in the xy plane to mimic the experimental conditions to which we compare our results (see Experimental methods). We performed production in the *NPT* ensemble with C-rescale barostat and semi-isotropic coupling at a pressure of 1 bar in the z dimension and −10 bar in xy. We first made a 2D slab configuration at 300 K with no scaling factor. Protein was added to form a continuous strip across the periodic boundary, resulting in a total of 120 chains. The system was then minimized, equilibrated and subject to a short production that allowed the proteins to condense to an equilibrium state. This slab was then used as the initial conformation for subsequent productions at varying temperatures and scaling factors. For each new temperature, a short equilibration was performed, followed by a production run of 10 μs, or until system convergence, as evaluated by protein density in the condensed phase. Initial conformations for additional repeats were taken from the final state of simulations with the same scaling factor, generating new velocities.

Experimental methods

Materials. 1,2-Dioleoyl-*sn-glycero*-3-phosphocholine (DOPC), 1,2-dioleoyl-*sn-glycero*-3-phospho-L-serine (DOPS), and 1,2-dioleoyl-*sn-glycero*-3-[(*N*-(5-amino-1-carboxypentyl)iminodiacetic acid)succinyl] nickel salt (DGS-Ni-NTA) were purchased from Avanti Polar Lipids. Texas Red 1,2-dihexadecanoyl-*sn-glycero*-3-phosphoethanolamine triethylammonium salt (Texas Red-

DHPE), and 4-(2-hydroxyethyl)-1-piperazineethanesulfonic acid (HEPES) were purchased from Thermo Fisher Scientific. Sodium chloride, sodium tetraborate, hexadecane, silicone oil AR 20, poly-L-lysine MW 15 000–30 000 (PLL), Atto 488 NHS ester was purchased from Sigma-Aldrich. Amine-reactive PEG (mPEG–succinimidyl valerate, MW 5000) was purchased from Laysan Bio.

Plasmids. The plasmid for the RGG (pET-RGG) was a gift from Matthew Good, Daniel Hammer, and Benjamin Schuster (Addgene plasmid #124929; https://www.addgene.org/124929).[50]

Protein expression and purification. Expression and purification of RGG protein was performed as described previously.[50] Briefly, *E. coli* BL21(DE3) competent cells were transformed with a plasmid encoding RGG. After transformation, cells were grown in 1 L of 2× YT media for 3–4 hours at 37 °C while shaking at 220 rpm until the optical density at 600 nm (OD_{600}) of the media became reached 0.8, followed by overnight expression induced with 0.5 mM of isopropyl β-D-1-thiogalactopyranoside (IPTG) at 18 °C while shaking at 220 rpm. Pellets of cells expressing RGG were harvested through centrifugation at 4 °C. Pellets were resuspended in 40 mL buffer containing 20 mM Tris, 500 mM NaCl, 20 mM imidazole, 1% Triton X-100, and one EDTA-free protease inhibitor tablet (Sigma Aldrich) at pH 7.5, and lysed by sonication on ice. To prevent the formation of RGG condensates, all of the following steps were done at room temperature. The cell lysate was clarified by centrifugation at 15 000*g* for 30 min and then incubated with Ni-NTA resin (G Biosciences, USA) for 1 hour to enable protein binding *via* histidine–nickel interactions, as RGG has a C-terminal histidine tag. Protein-bound Ni-NTA resin was settled in a glass column and washed with a buffer containing 20 mM Tris, 500 mM NaCl, and 20 mM imidazole at pH 7.5. The bound proteins were eluted from the Ni-NTA resin with a buffer containing 20 mM Tris, 500 mM NaCl, and 500 mM imidazole at pH 7.5. Eluted proteins were then exchanged into the storage buffer (20 mM Tris, 500 mM NaCl, pH 7.5). Small aliquots of the protein were flash-frozen using liquid nitrogen and stored at −80 °C.

Protein labeling. For visualization, RGG was labeled with the amine-reactive Atto 488 NHS ester. The labeling reaction took place in its storage buffer (25 mM HEPES, 500 mM NaCl, pH 7.5). Dye was added to the protein in 2-fold stoichiometric excess and allowed to react for 30 min at room temperature. Labeled protein was separated from unconjugated dye using Amicon Ultra 0.5 mL centrifugal filters with MWCO of 3k. The labeling ratio was measured using UV-vis spectroscopy. Labeled proteins were dispensed into small aliquots, flash-frozen in liquid nitrogen, and stored at −80 °C.

Suspended planar lipid membrane formation. Lipids dissolved in chloroform were mixed in a glass vial and dried under a gentle N_2 stream. The dried lipid film was redissolved in a mixture of hexadecane and silicone oil (1 : 1, v/v) to obtain a lipid/oil solution with a total lipid concentration of 3 mM. Each oil was filtered through a 0.2 μm syringe filter (Corning Inc.) before use. The lipid/oil solution was bath-sonicated for 30 min and used for experiments within several hours. The glass coverslip of the imaging chamber was passivated with a layer of PLL–PEG, which was synthesized as described previously.[28,40] A total of 100–150 μL of the aqueous buffer was then added into the imaging chamber. After that, 1–2 μL of lipid/oil solution was gently dropped and spread on the air–aqueous buffer interface. After several minutes, a hexagonal TEM grid made of gold (G150HEX Au, Gilder Grids, 150 μm of hole width), which was hydrophobically coated by incubating in 1-dodecanethiol solution (5 mM dissolved in ethanol) overnight before use, was gently placed on the air–oil interface using tweezers. After several minutes, the grid was submerged into the aqueous buffer using a syringe needle to place it on the PLL–PEG-coated glass surface. The thickness of the oil film decreased as the oil drained out, and spontaneous adhesion of two lipid monolayers occurred, resulting in a suspended planar lipid bilayer. Proteins were added at a concentration of 1 μM above the lipid bilayer.

Microscopy. A spinning disk confocal microscope (SpinSR10, Olympus) equipped with a Hamamatsu Orca Flash 4.0 V3 sCMOS Digital Camera was used to visualize samples. 1.40 NA/40× oil immersion objective (1-UXB220, Olympus) was used for visualization. Laser wavelength of 488 nm was used for excitation.

Image analysis. ImageJ was used for image analysis. For all cases, fluorescence intensity values were measured in unprocessed images. To measure partition coefficients (K_P) of proteins, fluorescence intensity values (background subtracted) of two adjacent brighter and dimmer regions were used to avoid the effect of local variations in intensity.

Author contributions

KZ contributed conceptualization, formal analysis, investigation, visualization, and writing. SP and NP contributed to investigation. YL contributed formal analysis, investigation, visualization, and writing. PR and JSC contributed conceptualization, formal analysis, investigation, funding acquisition, supervision, and writing.

Conflicts of interest

There are no conflicts to declare.

Data availability

Trajectories used for data analysis are available on zenodo at https://doi.org/10.5281/zenodo.15785473.

The data supporting this article, including simulation input files, have been included as part of the SI. See DOI: https://doi.org/10.1039/d5sc04862a.

Acknowledgements

PR thanks the support from the Welch Foundation under F-2120. JSC acknowledges support from the National Institutes of Health under R35GM139531, including a supplement to support KZ, and from the Welch Foundation under F-2257. PR and JSC additionally thank support from NSF BIO under 2529782. KZ further acknowledges a graduate research fellowship from the National Science Foundation.

References

1 S. Alberti, A. Gladfelter and T. Mittag, Considerations and Challenges in Studying Liquid-Liquid Phase Separation and Biomolecular Condensates, *Cell*, 2019, **176**(3), 419–434.

2 G. L. Dignon, R. B. Best and J. Mittal, Biomolecular Phase Separation: From Molecular Driving Forces to Macroscopic Properties, *Annu. Rev. Phys. Chem.*, 2020, **71**, 53–75.

3 C. P. Brangwynne, P. Tompa and R. V. Pappu, Polymer physics of intracellular phase transitions, *Nat. Phys.*, 2015, **11**(11), 899–904.

4 A. S. Holehouse and B. B. Kragelund, The molecular basis for cellular function of intrinsically disordered protein regions, *Nat. Rev. Mol. Cell Biol.*, 2024, **25**(3), 187–211.

5 R. van der Lee, M. Buljan, B. Lang, R. J. Weatheritt, G. W. Daughdrill, A. K. Dunker, *et al.*, Classification of Intrinsically Disordered Regions and Proteins, *Chem. Rev.*, 2014, **114**(13), 6589–6631.

6 P. E. Wright and H. J. Dyson, Intrinsically disordered proteins in cellular signalling and regulation, *Nat. Rev. Mol. Cell Biol.*, 2015, **16**(1), 18–29.

7 Y. Shin and C. P. Brangwynne, Liquid phase condensation in cell physiology and disease, *Science*, 2017, **357**(6357), eaaf4382.

8 C. W. Pak, M. Kosno, A. S. Holehouse, S. B. Padrick, A. Mittal, R. Ali, *et al.*, Sequence Determinants of Intracellular Phase Separation by Complex Coacervation of a Disordered Protein, *Mol. Cell*, 2016, **63**(1), 72–85.

9 M. T. Wei, S. Elbaum-Garfinkle, A. S. Holehouse, C. C. H. Chen, M. Feric, C. B. Arnold, *et al.*, Phase behaviour of disordered proteins underlying low density and high permeability of liquid organelles, *Nat. Chem.*, 2017, **9**(11), 1118–1125.

10 G. Krainer, T. J. Welsh, J. A. Joseph, J. R. Espinosa, S. Wittmann, E. de Csilléry, *et al.*, Reentrant liquid condensate phase of proteins is stabilized by hydrophobic and non-ionic interactions, *Nat. Commun.*, 2021, **12**(1), 1085.

11 W. T. Snead and A. S. Gladfelter, The Control Centers of Biomolecular Phase Separation: How Membrane Surfaces, PTMs, and Active Processes Regulate Condensation, *Mol. Cell*, 2019, **76**(2), 295–305.

12 F. Yuan, H. Alimohamadi, B. Bakka, A. N. Trementozzi, K. J. Day, N. L. Fawzi, *et al.*, Membrane bending by protein phase separation, *Proc. Natl. Acad. Sci. U. S. A.*, 2021, **118**(11), e2017435118.

13 W. T. Snead, A. P. Jalihal, T. M. Gerbich, I. Seim, Z. Hu and A. S. Gladfelter, Membrane surfaces regulate assembly of ribonucleoprotein condensates, *Nat. Cell Biol.*, 2022, **24**(4), 461–470.

14 D. B. McAffee, M. K. O'Dair, J. J. Lin, S. T. Low-Nam, K. B. Wilhelm, S. Kim, *et al.*, Discrete LAT condensates encode antigen information from single pMHC:TCR binding events, *Nat. Commun.*, 2022, **13**(1), 7446.

15 X. Su, J. A. Ditlev, E. Hui, W. Xing, S. Banjade, J. Okrut, *et al.*, Phase separation of signaling molecules promotes T cell receptor signal transduction, *Science*, 2016, **352**(6285), 595–599.

16 C. W. Lin, L. M. Nocka, B. L. Stinger, J. B. DeGrandchamp, L. J. N. Lew, S. Alvarez, *et al.*, A two-component protein condensate of the EGFR cytoplasmic tail and Grb2 regulates Ras activation by SOS at the membrane, *Proc. Natl. Acad. Sci. U. S. A.*, 2022, **119**(19), e2122531119.

17 O. Beutel, R. Maraspini, K. Pombo-García, C. Martin-Lemaitre and A. Honigmann, Phase Separation of Zonula Occludens Proteins Drives Formation of Tight Junctions, *Cell*, 2019, **179**(4), 923–936.

18 K. Pombo-García, O. Adame-Arana, C. Martin-Lemaitre, F. Jülicher and A. Honigmann, Membrane prewetting by condensates promotes tight-junction belt formation, *Nature*, 2024, **632**(8025), 647–655.

19 M. Kozak and M. Kaksonen, Condensation of Ede1 promotes the initiation of endocytosis, *eLife*, 2022, **11**, e72865.

20 K. J. Day, G. Kago, L. Wang, J. B. Richter, C. C. Hayden, E. M. Lafer, *et al.*, Liquid-like protein interactions catalyse assembly of endocytic vesicles, *Nat. Cell Biol.*, 2021, **23**(4), 366–376.

21 F. Campelo, J. V. Lillo and J. von Blume, Protein condensates in the secretory pathway: Unraveling biophysical interactions and function, *Biophys. J.*, 2024, **123**(12), 1531–1541.

22 A. Parchure, M. Tian, D. Stalder, C. K. Boyer, S. C. Bearrows, K. E. Rohli, J. Zhang, F. Rivera-Molina, B. R. Ramazanov, S. K. Mahata, Y. Wang, S. B. Stephens, D. C. Gershlick and J. von Blume, Liquid–liquid phase separation facilitates the biogenesis of secretory storage granules, *J. Cell Biol.*, 2022, **221**(12), e202206132.

23 A. Johnson, N. Bhattacharya, M. Hanna, J. G. Pennington, A. L. Schuh, L. Wang, *et al.*, TFG clusters COPII-coated transport carriers and promotes early secretory pathway organization, *EMBO J.*, 2015, **34**(6), 811–827.

24 M. G. Hanna, S. Block, E. B. Frankel, F. Hou, A. Johnson, L. Yuan, *et al.*, TFG facilitates outer coat disassembly on COPII transport carriers to promote tethering and fusion with ER–Golgi intermediate compartments, *Proc. Natl. Acad. Sci. U. S. A.*, 2017, **114**(37), E7707–E7716.

25 S. A. Tooze, G. J. M. Martens and W. B. Huttner, Secretory granule biogenesis: rafting to the SNARE, *Trends Cell Biol.*, 2001, **11**(3), 116–122.

26 H. Y. Wang, S. H. Chan, S. Dey, I. Castello-Serrano, M. K. Rosen, J. A. Ditlev, *et al.*, Coupling of protein condensates to ordered lipid domains determines functional membrane organization, *Sci. Adv.*, 2023, **9**(17), eadf6205.

27 A. Mangiarotti, M. Siri, N. W. Tam, Z. Zhao, L. Malacrida and R. Dimova, Biomolecular condensates modulate membrane lipid packing and hydration, *Nat. Commun.*, 2023, **14**(1), 6081.

28 Y. Lee, S. Park, F. Yuan, C. C. Hayden, L. Wang, E. M. Lafer, *et al.*, Transmembrane coupling of liquid-like protein condensates, *Nat. Commun.*, 2023, **14**(1), 8015.

29 Z. Benayad, S. von Bülow, L. S. Stelzl and G. Hummer, Simulation of FUS Protein Condensates with an Adapted Coarse-Grained Model, *J. Chem. Theory Comput.*, 2021, **17**(1), 525–537.

30 S. Mondal and Q. Cui, Coacervation of poly-electrolytes in the presence of lipid bilayers: mutual alteration of structure and morphology, *Chem. Sci.*, 2022, **13**(26), 7933–7946.

31 M. M. Anila, R. Ghosh and B. Różycki, Membrane curvature sensing by model biomolecular condensates, *Soft Matter*, 2023, **19**(20), 3723–3732.

32 R. Ghosh, V. Satarifard and R. Lipowsky, Different pathways for engulfment and endocytosis of liquid droplets by nanovesicles, *Nat. Commun.*, 2023, **14**(1), 615.

33 S. Elbaum-Garfinkle, Y. Kim, K. Szczepaniak, C. C. H. Chen, C. R. Eckmann, S. Myong, *et al.*, The disordered P granule protein LAF-1 drives phase separation into droplets with tunable viscosity and dynamics, *Proc. Natl. Acad. Sci. U. S. A.*, 2015, **112**(23), 7189–7194.

34 P. C. T. Souza, R. Alessandri, J. Barnoud, S. Thallmair, I. Faustino, F. Grünewald, *et al.*, Martini 3: a general purpose force field for coarse-grained molecular dynamics, *Nat. Methods*, 2021, **18**(4), 382–388.

35 S. J. Marrink and D. P. Tieleman, Perspective on the Martini model, *Chem. Soc. Rev.*, 2013, **42**(16), 6801–6822.

36 F. E. Thomasen, F. Pesce, M. A. Roesgaard, G. Tesei and K. Lindorff-Larsen, Improving Martini 3 for Disordered and Multidomain Proteins, *J. Chem. Theory Comput.*, 2022, **18**(4), 2033–2041.

37 A. Claveras Cabezudo, C. Athanasiou, A. Tsengenes and R. C. Wade, Scaling Protein–Water Interactions in the Martini 3 Coarse-Grained Force Field to Simulate Transmembrane Helix Dimers in Different Lipid Environments, *J. Chem. Theory Comput.*, 2023, **19**(7), 2109–2119.

38 J. Cornish, S. G. Chamberlain, D. Owen and H. R. Mott, Intrinsically disordered proteins and membranes: a marriage of convenience for cell signalling?, *Biochem. Soc. Trans.*, 2020, **48**(6), 2669–2689.

39 T. Das and D. Eliezer, Membrane interactions of intrinsically disordered proteins: The example of alpha-synuclein, *Biochim. Biophys. Acta, Proteins Proteomics*, 2019, **1867**(10), 879–889.

40 H. R. Lee, Y. Lee, S. S. Oh and S. Q. Choi, Ultra-Stable Freestanding Lipid Membrane Array: Direct Visualization of Dynamic Membrane Remodeling with Cholesterol Transport and Enzymatic Reactions, *Small*, 2020, **16**(40), e2002541.

41 S. J. Marrink, H. J. Risselada, S. Yefimov, D. P. Tieleman and A. H. de Vries, The MARTINI Force Field: Coarse Grained Model for Biomolecular Simulations, *J. Phys. Chem. B*, 2007, **111**(27), 7812–7824.

42 D. Van Der Spoel, E. Lindahl, B. Hess, G. Groenhof, A. E. Mark and H. J. C. Berendsen, GROMACS: fast, flexible, and free, *J. Comput. Chem.*, 2005, **26**(16), 1701–1718.

43 M. J. Abraham, T. Murtola, R. Schulz, S. Páll, J. C. Smith, B. Hess, *et al.*, GROMACS: High performance molecular simulations through multi-level parallelism from laptops to supercomputers, *SoftwareX*, 2015, **1–2**, 19–25.

44 Schrödinger, LLC, *The PyMOL Molecular Graphics System, Version 1.8*, 2015.

45 J. Jumper, R. Evans, A. Pritzel, T. Green, M. Figurnov, O. Ronneberger, *et al.*, Highly accurate protein structure prediction with AlphaFold, *Nature*, 2021, **596**(7873), 583–589.

46 P. C. Kroon, F. Grunewald, J. Barnoud, M. van Tilburg, P. C. T. de Souza, T. A. Wassenaar, *et al.*, Martinize2 and Vermouth: Unified Framework for Topology Generation, *eLife*, 2024, **12**, RP90627.

47 T. A. Wassenaar, H. I. Ingólfsson, R. A. Böckmann, D. P. Tieleman and S. J. Marrink, Computational Lipidomics with insane: A Versatile Tool for Generating Custom Membranes for Molecular Simulations, *J. Chem. Theory Comput.*, 2015, **11**(5), 2144–2155.

48 S. Jo, T. Kim, V. G. Iyer and W. Im, CHARMM-GUI: A web-based graphical user interface for CHARMM, *J. Comput. Chem.*, 2008, **29**(11), 1859–1865.

49 Y. Qi, H. I. Ingólfsson, X. Cheng, J. Lee, S. J. Marrink and W. Im, CHARMM-GUI Martini Maker for Coarse-Grained Simulations with the Martini Force Field, *J. Chem. Theory Comput.*, 2015, **11**(9), 4486–4494.

50 B. S. Schuster, E. H. Reed, R. Parthasarathy, C. N. Jahnke, R. M. Caldwell, J. G. Bermudez, *et al.*, Controllable protein phase separation and modular recruitment to form responsive membraneless organelles, *Nat. Commun.*, 2018, **9**(1), 2985.